Integrating an SW-LSTM Model with GNSS-IR to Enhance Sea-Level Measurements during Storm Surges

Kailun Hu, Dongju Peng, Linlin Li and Huabin Shi

***Abstract*—Conventional tide gauges have limitations in extreme weather due to their susceptibility to damage from high waves and storm surges, as well as potential inaccuracies caused by rapid changes in wind speed and atmospheric pressure. To overcome these potential issues, Global Navigation Satellite System-interferometric reflectometry (GNSS-IR) is adopted for detecting storm surges as a supplement part of observation systems. The current GNSS-IR technique has insufficient accuracy and temporal resolution to capture high storm surge. In this study, we develop a sliding-window-based Long Short Term Memory (SW-LSTM) framework to post-process GNSS-IR retrieval results. Three scenarios of the SW-LSTM model are proposed in terms of the prior information involved as input features into LSTM networks. The models are validated in the inversion of sea levels in Quarry Bay of Hong Kong during typhoons Hato, Khanun, Mangkhut, Wipha, and Kompasu. The RMSEs in the GNSS-IR retrieval results are between 15.0 cm and 18.8 cm and the skill scores vary between 0.963 and 0.979. The data during Mangkhut, Wipha and Kompasu are adopted to train the SW-LSTM models. After post-processing with the SW-LSTM models, the RMSE in the obtained sea levels is reduced to 6.8 cm for the Super Typhoon Hato and 6.5 cm for the Severe Typhoon Khanun. The skill scores are all above 0.990. Moreover, a comparison analysis shows that the SW-LSTM models outperform the least squares method and the cubic spline interpolation for GNSS-IR retrieval improvement. The SW-LSTM models show potential to extend GNSS-IR altimetry to real-time monitoring and synchronous predictions.**

***Index Terms*—Global navigation satellite system reflectometry (GNSS-R), signal-to-noise ratio (SNR), sea-level measurement, machine learning method, sliding-window long short-term memory model (SW-LSTM), storm surge.**

I. Introduction

A storm surge is an abnormal rise in sea level that occurs during tropical cyclones (Fritz et al., 2007; Soria et al., 2016). It can result in severe coastal flooding, posing a significant threat to coastal infrastructure, economy, and human lives. For example, the estimated economic loss resulting from storm surges in the Guangdong-Hong Kong-Macao Greater Bay Area in the past decade exceeded 20 billion CNY. Furthermore, storm surges are likely to intensify as a result of global warming [3], [4]. It is thus important to monitor storm surges to enhance preparedness and minimize potential losses. Tide gauges are widely used to measure the fluctuations in sea level during storm surges [5]-[7]. However, tide gauges may experience malfunction during extreme events as they must be installed close to water and are susceptible to damage. As an example, in Macau, all gauges were not properly functioning during the Super Typhoon Hato because of damage or interruption in electricity supply [8]-[10].

Over the past decade, global navigation satellite system interferometric reflectometry (GNSS-IR) has been emerging as an in-situ sea-level observing technique [11], [12]. Compared to conventional tide gauges, it has advantages of (1) being less likely damaged during extreme events because GNSS-IR stations can be installed at a relatively high location such as roof top so as to reduce the risk of being damaged during storms; (2) sensing changes of the sea surface in a large zone extending tens to hundreds of meters from the coast [13], [14]; and (3) simultaneously measuring the relative sea levels that conventional tide gauges record and land-height changes [15], [16]. Despite those advantages, GNSS-IR sea-level measurements have limitations in terms of temporal resolution and accuracy of individual measurements, particularly under extreme weather (e.g., Super Typhoons). In this study, we aim to improve the accuracy and temporal resolution of GNSS-IR sea-level measurements during extreme events by using a deep learning method, i.e., Long-Short Term Memory (LSTM) network.

LSTM networks are a subclass of recurrent neural networks (RNNs) designed to effectively address sequential data. They have been demonstrated to outperform traditional RNN in

The research is jointly supported by the National Key Research and Development Program of China (Grant No. 2023YFC3008600), the Jiangyin Hi-tech Industrial Development Zone (JOIND) under the Taihu Innovation Scheme (EF2025-00004-SKL-IOTSC), the Science and Technology Development Fund, Macau S.A.R. (File no. 001/2024/SKL, 0101/2024/AMJ), and Multi-Year Research Grant of University of Macau (No. MYRG-GRG2024-00182-IOTSC). D.P. acknowledges support from PolyU Research Funds (Project IDs: P0048429 and ZH8Y) and Hong Kong RGC Collaborative Research Fund (C5013-23G). (Corresponding authors: H. Shi and D. Peng)

K. Hu is with the State Key Laboratory of Internet of Things for Smart City and Department of Ocean Science and Technology, University of Macau, Macao, China (e-mail: yc47935@um.edu.mo).

D. Peng is with Department of Land Surveying and Geo-Informatics, The Hong Kong Polytechnic University, Kowloon, Hong Kong SAR, China (e-mail: dongju.peng@polyu.edu.hk).

L. Li is with Guangdong Provincial Key Laboratory of Geodynamics and Geohazards, School of Earth Sciences and Engineering, Sun Yat-Sen University, Zhuhai 519080, China (e-mail: lilinlin3@mail.sysu.edu.cn).

H. Shi is with State Key Laboratory of Internet of Things for Smart City and Department of Ocean Science and Technology, University of Macau, Macao, China & Zhuhai UM Science & Technology Research Institute, Zhuhai, China (e-mail: huabinshi@um.edu.mo).

handling complex and dynamic tasks because of their ability to manage long-term dependencies in sequential data [17], [18]. LSTMs have been widely used in various fields, including stock price prediction [18], [19], disease screening [20] and prediction of extreme floods [21]. Building on the capabilities of standard LSTM, advanced models such as recurrent deep neural combined feature attention mechanism (FA-RDN) and time-aware long short-term memory model anomaly detection (T-LSTM-AD) have been developed to enhance various GNSS-related applications. For example, FA-RDN has been applied to improve the observation of sea surface wind speed based on GNSS-R retrievals [22]. Similarly, T-LSTM-AD has been used to improve GNSS-IR sea-level estimates at a site with a tidal range less than 60 cm by detecting outliers and correcting the effect of dynamic sea surface variations [23]. Given that errors in GNSS-IR sea-level estimates are positively related to tidal ranges [11], [24] further investigation is needed to assess the effectiveness of LSTM in improving GNSS-IR sea-level estimates at locations with larger tidal ranges. Additionally, the effectiveness of LSTM during extreme sea-level events, such as storm surges, has not been reported yet. In this study, we aim to develop an advanced LSTM model, specifically sliding window LSTM (SW-LSTM), to further process the GNSS-IR sea-level estimates derived from the signal-to-noise ratio (SNR) data by using lomb-scargle periodogram (LSP), with the goal of improving sea-level measurements during storm surges.

Sufficient temporal resolution is key to optimizing the performance of the SW-LSTM model, as data gaps can lead to the faults of calculation [25]. To achieve the highest possible temporal resolution, we use SNR data from multiple constellations and multiple frequencies to derive GNSS-IR sea-level estimates. This approach has been proven to significantly enhance temporal resolution when compared to deriving sea-level estimates from a single GNSS constellation [26]-[29]. To evaluate the performance of our SW-LSTM model, we consider three different scenarios. The first scenario uses adjacent GNSS-IR sea-level estimates to match an available value at each moment. This method bases on the uneven resolution and indeterminacy of GNSS-IR data to provide continuous sea-level measurements. The second scenario incorporates astronomical tides as an additional factor to improve the estimates by accounting for predictable tidal influences on dynamic sea surface. This approach enhances the model's ability to predict sea-level changes influenced by tidal patterns. The third scenario integrates tide-gauge measurements with our model to significantly enhance accuracy, serving as a supplementary method during short-term tide-gauge outages. This integration ensures the reliability of sea-level estimates even when direct measurements are temporarily unavailable. Those three scenarios are representative of typical installation conditions that account for coastal tidal factors, allowing us to assess the robustness of the SW-LSTM model across varying conditions (details in section 3.3).

II. Data

To evaluate our model, we used the GNSS data from the HKQT station in Hong Kong. The geographic location and photography of HKQT station are shown in Figure 1. This site is equipped with a TRIMBLE NETR9 receiver and a TRM57971.00 antenna, receiving signals from GPS, GLONASS, Galileo, BeiDou, and SBAS. In our study, we used data at a 30-second sampling interval from 12 frequencies, including L1, L2, L5 of GPS; G1, G2 of GLONASS; E1, E5a, E5b, E5 (E5a+E5b) of Galileo; as well as B1, B2, B3 of BeiDou. The inter-frequency bias is not considered in this study because its magnitude is small compared to the errors [30]. The details of constellations and frequencies are shown in Table 1. To restrict signals from the land, we applied an elevation angle mask of 4˚ to 10˚ and an azimuth mask between − 55˚ and 90˚. Since our focus is on improving sea-level measurements during storm surges in terms of both temporal resolution and accuracy, we selected the data during five recent typhoons, i.e., Super Typhoon Hato (1713), Severe Typhoon Khanun (1720), Super Typhoon Mangkhut (1822), Tropical Storm Wipha (1907) and Typhoon Kampasu (2118), for analysis. A conventional tide gauge is co-located with this GNSS site. The hourly data of sea level recorded by this tide gauge were utilized to validate the model. The predicted astronomical tide from harmonic analysis by the Hong Kong Observatory, which were at a 15-minute sampling interval, was used to enhance our post-processing method

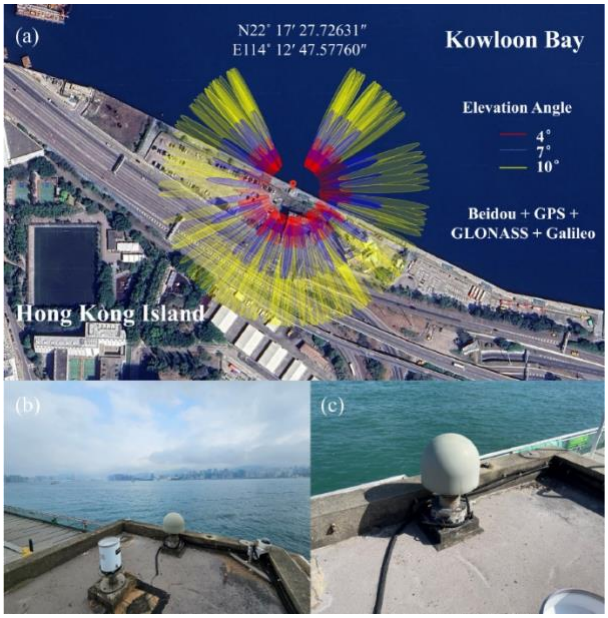

Fig. 1. A top-down view of the reflection zones from https://gnss-reflections.org/rzones [13] (a), and photos of the GNSS equipment (b and c) from the Hong Kong Satellite Positioning Reference Station Network (SatRef).

TABLE I
ADOPTED SATELLITE SYSTEMS, FREQUENCY BANDS, FREQUENCY OF GNSS RECEIVER IN HKQT STATION, AND ITS PSEUDORANGE CODE, PHASE CODE, AND SNR CODE OF EACH SIGNALS.

Satellite system	Frequency band	Frequency	Signal	Pseudorange code	Phase code	SNR code
GPS	L1	1575.42	C/A	C1C	L1C	S1C
	L2	1227.60	C/A	C2C	L2C	S2C
	L5	1176.45	I+Q	C5X	L5X	S5X
GLONASS	G1	1602 + k × 9/16 k = −7, ..., 11, 12	C/A	C1C	L1C	S1C
	G2	1246+k×7/16	C/A	C2C	L2C	S2C
Galileo	E1	1575.42	B+C	C1X	L1X	S1X
	E5a	1176.45	I+Q	C5X	L5X	S5X
	E5b	1207.140	I+Q	C7X	L7X	S7X
	E5 (E5a+E5b)	1191.795	I+Q	C8X	L8X	S8X
BeiDou	B1l	1561.098	I	C2I	L2I	S2I
	B2b	1207.14	I	C7I	L7I	S7I
	B3l	1268.52	I	C6I	L6I	S6I

III. METHODS

A. GNSS SNR Data Processing

As illustrated in Figure 2, a land-based GNSS antenna placed near the coast receives signal directly from the satellites as well as those reflected off the nearby water surface. These two signals interfere with each other, resulting in an oscillating pattern overlain on a long-time trend in the SNR data. The frequency of these oscillations is linked to the reflector height (h) and can be determined from the SNR residuals (δSNR) following the equation proposed by [10] as below:

$$\delta\mathrm{SNR} = A\cos\left[\frac{4\pi h}{\lambda}\sin(\varepsilon)+\varphi\right] \quad (1)$$

where A is the amplitude of multipath oscillations; ε is the elevation angle of satellite; λ is the wavelength of GNSS signals; and φ is a phase offset. The SNR residuals are obtained by applying a third-order polynomial to remove the trend.

We used the gnssrefl software package [31] to process SNR data and derive reflector heights using LSP. Subtracting h from the height of the GNSS antenna (relative to the local mean sea level), we obtained the sea level, which is notated ξ and hereafter named LSP sea level. To address the tropospheric delays affecting the reflected signals, which are typically recognized as scale errors that decrease exponentially with satellite elevation angle and increase linearly with reflector height [15], [32]-[34], we employed a combination of an astronomical refraction model [35] and Global Pressure and Temperature 2 (GPT2) Wet model [36] to correct the biases caused by these delays. This approach can largely correct the tropospheric delays [33], [37]. Moreover, the dynamic nature of sea surface cause biases in the reflector height due to height-rate change over a satellite pass, which need to be mitigated to improve GNSS-IR sea-level estimates [11]. Under normal weather conditions, these biases can be largely corrected by iteratively estimating astronomical tides and using the predicted tides to account for the height-rate change [11], [26]. However, during storm surges, sea levels can deviate significantly from astronomical tides, making this method potentially ineffective. Therefore, here we chose not to apply this correction.

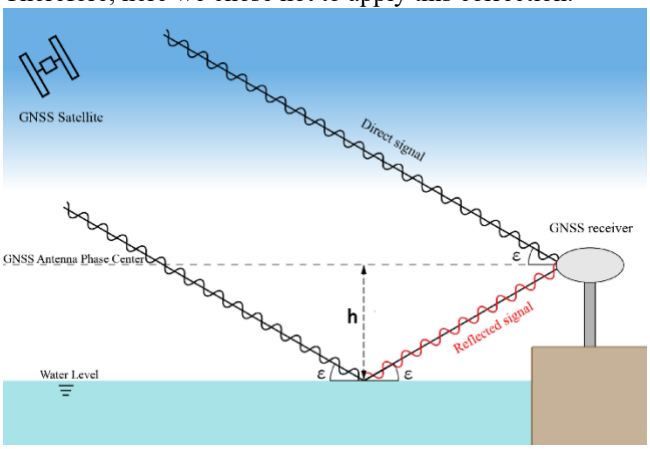

Fig. 2. Sketch of the GNSS-IR principle.

B. The SW-LSTM model

The discrete data points of sea levels obtained using the LSP method are generally highly irregularly distributed over time. To obtain a smooth and continuous curve with a fixed temporal resolution, an SW-LSTM model is proposed to post-process the LSP sea levels. Figure 3 shows the framework of the SW-LSTM model. The model is composed of two parts: a multi-layer LSTM neural network and a data-combination component using the sliding window. The target variable of the data samples for the multi-layer LSTM neural network is the processed sea level at a target instant t, as shown in Figure 3. The input features of a data sample include the LSP sea levels within the sliding window centered on the target instant t as well as some prior information like the astronomical tidal levels. Notably, the prior information is introduced to improve

the prediction accuracy of the SW-LSTM model. The multi-dimensional features are integrated in the data-combination component of the proposed framework.

1) The multi-layer LSTM neural network: In this study, the network consists of two LSTM layers and two dense layers, as shown in Figure 3. In each layer, there are a series of connected neurons that are the basic structure of neural networks. Generally, the number of neurons in a layer is a power of 2 (e.g., 32, 64, 128) which is favorable to parallel computing and hardware optimization. In each neuron of the LSTM layer, the recurrent unit, which is denoted by the letter A in Figure 3, plays a critical role in capturing the temporal dependencies among sequential data. To address the problems of vanishing gradient and inability to learn the long-term dependencies in traditional RNNs, the gate mechanism is introduced into LSTM networks. Accordingly, a recurrent unit of a LSTM network consists of a memory cell, a forget gate, an input gate, and an output gate.

The memory cell is adopted to store info from previous steps. Its state at the i-th step, represented by a parameter C_i, is utilized to quantify the info stored. The forget gate is used to determine what information from the previous cell state C_{i-1} should be discarded, while the input gate is introduced to determine what new information be added to the memory cell. Accordingly, the state at the i-th step is updated as

$$C_i = f_i C_{i-1} + i_i \hat{C}_i \tag{2}$$

$$\hat{C}_i = \tanh\left(W_{Cx} x_i + W_{Ch} h_{i-1} + b_C\right) \tag{3}$$

where $\hat{C}_i$ is an intermediate value of the cell state; f_i is the outcome of the forget gate at the *i*-th step and i_i is that of the input gate; x_i is the input at the *i*-th step; h_{i-1} is the result from the hidden layer of the previous step $i-1$; W_{Cx} and W_{Ch} are weight matrices; b_C is a bias vector. Involving the hidden layer result h_{i-1} in the calculation is the key to enabling the neural network to handle the temporal dependency among sequential data. The result of the forget gate f_i varies in the range of $0 \sim 1$ and is calculated as

$$f_i = \sigma\left(W_{fx} x_i + W_{fh} h_{i-1} + b_f\right) \tag{4}$$

where σ is the sigmoid activation function; W_{fx} and W_{fh} are weight matrices; and b_f is a bias vector. $f_i = 0$ means that the previous cell state is completely forgot and discarded, while $f_i = 1$ indicates that the info of the previous cell state is completely kept. The outcome of the input gate i_i also varies between 0 and 1 and is determined by a sigmoid activation function as follows

$$i_i = \sigma\left(W_{ix} x_i + W_{ih} h_{i-1} + b_i\right) \tag{5}$$

where W_{ix} and W_{ih} are weight matrices; and b_i is a bias vector.

The output gate is introduced to control the pieces of information in the current memory cell to output as the result of the hidden layer. The outcome of the output gate at the *i*-th step, notated O_i, is also a function of the current input data x_i and the previous results in the hidden layer h_{i-1}, expressed as

$$O_i = \sigma\left(W_{Ox} x_i + W_{Oh} h_{i-1} + b_O\right) \tag{6}$$

where W_{Ox} and W_{Oh} are weight matrices; and b_O is a bias vector. Accordingly, the result of the hidden layer at the *i*-th step, notated h_i, is calculated as

$$h_i = O_i \cdot \tanh\left(C_i\right). \tag{7}$$

Subsequently, the updated cell state C_i and hidden-layer result h_i are utilized in the succeeding calculations.

In this study, the proposed SW-LSTM model consists of two subsequent LSTM layers followed by two dense layers. The dense layers are introduced to further extract and integrate features from the outputs of LSTM layers as well as reduce the dimensionality of the outputs. The numbers of the LSTM and dense layers can be adjusted based on calibrations. Generally, a higher number of LSTM layers may help to capture more characteristics among data but increases the complexity of the network and hence the computational cost. There are 64 neurons in the first LSTM layer and 32 neurons in the second LSTM layer. 16 neurons are used in the first dense layer and 1 neuron is utilized in the second. Notably, progressively reducing the number of neurons involved in the network layers is favorable to lowering the risk of overfitting.

2) The data-combination component: As denoted by the blue dots in Figure 3, in general, the obtained data points of LSP sea levels are distributed highly non-uniformly. To acquire a deterministic value of sea level at the target moment t, all the LSP sea level data in the sliding window centered on t are input into the LSTM network. For the input of an LSTM network, it is generally required that the dimension of the data sample features should be fixed. However, the irregular distribution of LSP sea level data leads to variability in the number of data points within a sliding window, which does not meet the requirement for the input data structure of an LSTM network. To address this, we set a fixed dimension of input features and conducted padding.

In this SW-LSTM model, a data sample into the first LSTM layer corresponds to a sliding window. As shown in Figure 3, the sliding window is shifted at a time interval of Δt. In symbols, X_t represents the input features of the data sample corresponding to the *t*-th window centered on the moment T_t. X_t is obtained by integrating all the LSP sea level data in the window with other prior information (like the astronomical tidal level) and organized to be a $N \times 2$ matrix in the data-combination component. The first column of the matrix is the

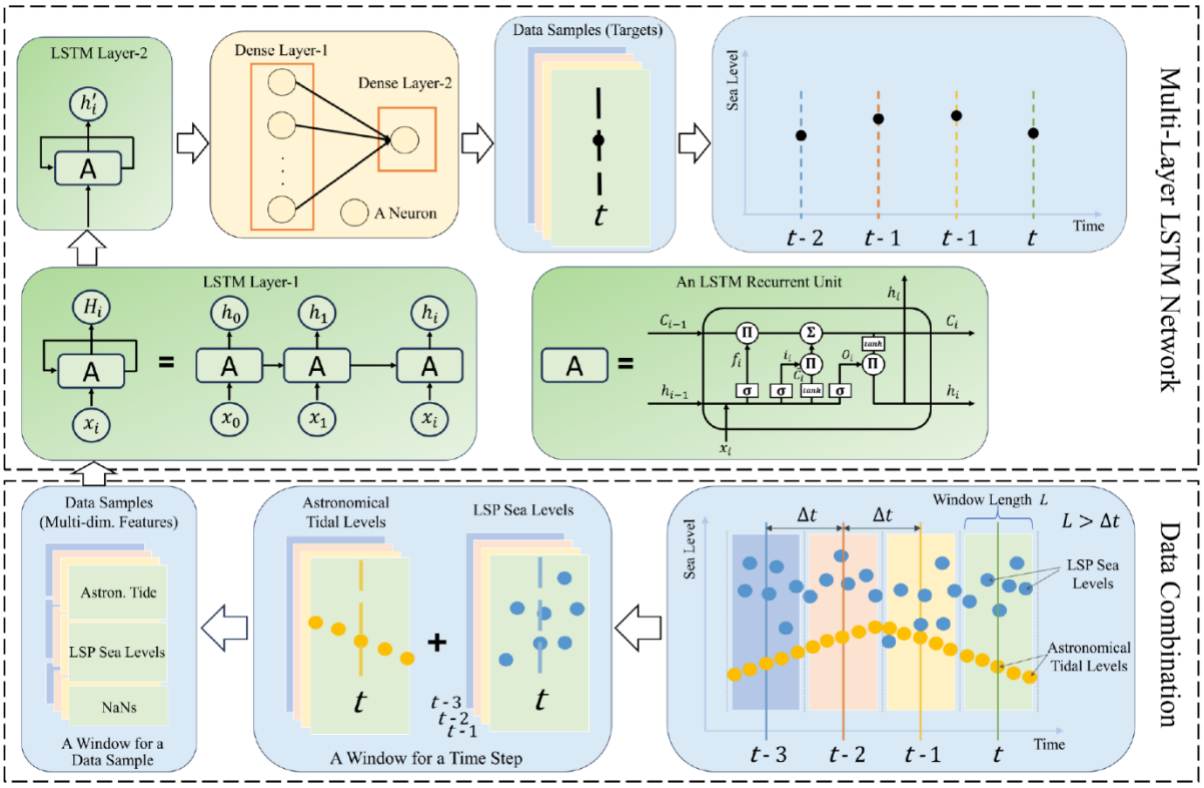

Fig. 3. Framework of the proposed SW-LSTM model for post-processing the LSP sea levels.

relative time of the data to the time T_t ,while the second column of the matrix contains the values of LSP sea level and the adopted prior information. The row number N is fixed in each application of the model and should be carefully set to ensure all the applicable date contained in the matrix. In a data sample, if the total number of the available data of LSP sea levels and the prior information is smaller than N , the matrix X_t is padded by null values (NaN). Consequently, the matrix X_t is generally composed of three parts and its structure is expressed as

$$X_t = \begin{bmatrix} A_t \\ B_t \\ \text{NULL} \end{bmatrix} \tag{8}$$

where A_t contains the prior information; B_t presents the data of LSP sea levels; and NULL is the padded NaN values. Further, the prior information part A_t is expressed as

$$A_t = \begin{bmatrix} \left(T'_{t,1} - T_t\right)/L & \eta_{t,1} \\ \left(T'_{t,2} - T_t\right)/L & \eta_{t,2} \\ \vdots & \vdots \\ \left(T'_{t,m} - T_t\right)/L & \eta_{t,m} \end{bmatrix} \tag{9}$$

where m is the number of the prior information data points within the t-th sliding window that is centered on the moment T_t and has a length of L; $T'_{t,1}, T'_{t,2}, \ldots, T'_{t,m}$ are the time of the prior information data and $\eta_{t,1}, \eta_{t,2}, \ldots, \eta_{t,m}$ are the values like the astronomical tidal level. The second part B_t contains all the LSP sea level data points within the i-th window and has a structure as

$$B_t = \begin{bmatrix} \left(T_{t,1} - T_t\right)/L & \xi_{t,1} \\ \left(T_{t,2} - T_t\right)/L & \xi_{t,2} \\ \vdots & \vdots \\ \left(T_{t,n} - T_t\right)/L & \xi_{t,n} \end{bmatrix} \tag{10}$$

where n is the number of the LSP sea level data points within the t-th sliding window; $T_{t,1}, T_{t,2}, \ldots, T_{t,n}$ are the time of the LSP sea level data points; $\xi_{t,1}, \xi_{t,2}, \ldots, \xi_{t,n}$ are the observed sea level values. The padding part NULL is a matrix of NaN values and has a dimension of $(N-m-n)\times 2$, expressed as

$$\text{NULL} = \begin{bmatrix} \text{NaN} & \text{NaN} \\ \text{NaN} & \text{NaN} \\ \vdots & \vdots \\ \text{NaN} & \text{NaN} \end{bmatrix}_{(N-m-n)\times 2} . \tag{11}$$

It is required that N must exceed $m+n$. In the applications, the value of N depends on the length of the sliding window L, the maximum possible number of LSP sea level data points in a window, and the number of the involved prior information data. One may expect a fixed extremely large value of N that can ensure it always exceeds $m+n$. However, regardless the

influence of too many NaN values on the model prediction accuracy, an excessively large N results in a significant increase in the model complexity and a decrease in the training and computational efficiency.

In terms of the adopted prior information, the SW-LSTM model can be applied to three scenarios, as shown in Figure 4. In the first scenario, no prior information is used and the SW-LSTM model relies solely on the LSP sea levels (Figure 4(a)). This approach is particularly beneficial in challenging environments where there is no prior information available. In the second scenario, the model can be enhanced by incorporating the predicted astronomical tides within the corresponding window as the prior information (Figure 4(b)), because tides account for a major part of sea-level variations under normal weather conditions. However, during extreme weather conditions, astronomical tides can differ significantly from the observed sea level. Therefore, in the third scenario, if observed data at neighboring tide gauges are available, the tide-gauge measurements before the target moment are integrated in the SW-LSTM model as prior information (Figure 4(c)). The previous tide-gauge measurements provide the real trend of sea level variation for the SW-LSTM model, which may reduce the prediction error of the LSTM network. This scenario can serve as a supplementary method to tide gauges in the event of short-duration power outages or breakdowns of tide-gauge station under extreme flooding.

In the applications of this study, the sliding window was shifted at an interval of $\Delta t = 15$ min. According to the sensitivity study presented in Section 4.3, the optimized length of the sliding window was $L = 4$ h. The maximum number of LSP sea level data points within a 4-hour-long window is lower than 51. Accordingly, we set the row number of B_t in a data sample to be $n = 51$. As illustrated in Figure 4(b), in the second scenario, an astronomical tidal level sequence with an time interval of 15 minutes predicted by the Hong Kong Observatory was included as the prior information. Consequently, there are 17 astronomical tide data points within a sliding window, including those at the boundaries of the window, and the row number of A_t in the data sample was set to be $m = 17$. In the third scenario (Figure 4(c)), an interpolated sequence of tide-gauge measured sea levels with an interval of 15 minutes was adopted as prior information. The number of the adopted tide-gauge data within a sliding widow is lower than 8 and the 17×2 matrix A_t is large enough to contain these data. Therefore, in the applications of this study, the row number of the data sample matrix X_t was set to $N = m + n = 68$. If the total number of LSP sea levels and prior information is smaller than 68, NaN values were padded at the end of the matrix X_t. In this study, the SW-LSTM model was applied to post-process the obtained LSP sea levels in a 7-day period during each of the five typhoons. In each typhoon, 665 sliding windows were adopted with a shifting interval of 15 minutes to cover the 7-day period. Accordingly, 665 data samples in each case of typhoon were acquired from the data-combination part of the SW-LSTM model. In total, 3325 data samples were available for the training and validation of the machine learning model.

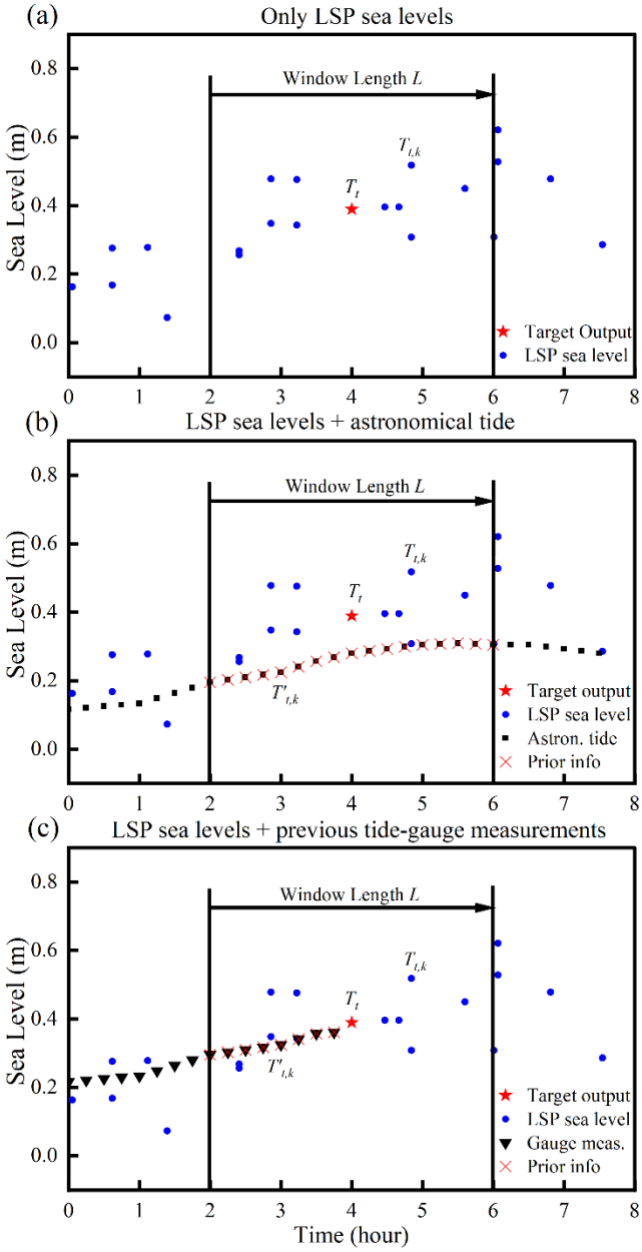

Fig. 4. Composition of the data sample in the three defined scenarios: (a) First scenario, only LSP sea levels and no prior information; (b) Second scenario, LSP sea levels and predicted astronomical tidal levels; (c) Third scenario, LSP sea levels and tide-gauge observed sea levels. The red star refers to the target output of the SW-LSTM model, the time of which is the central moment of the sliding window and represented by the symbol T_t. The blue dots are LSP sea levels, with the symbol $T_{t,k}$ representing the time of the k-th point in the t-th window. The symbol $T'_{t,k}$ denotes the time of the k-th astronomical tidal levels or the tide-gauge measured data points that are integrated into the data sample as prior information.

The matrices of data samples should be normalized before being put into the LSTM networks. Generally, normalization of

input data improves the stability of neural networks and mitigates the issues of vanishing or exploding gradient. Moreover, by ensuring consistent input data scaling, normalization of input features makes the optimization process more efficient and can significantly reduce the training time. The Min-Max scaling normalization was adopted in this study, of which the equation is expressed as

$$x^* = \frac{x - x_{\min}}{x_{\max} - x_{\min}}(\mathrm{Max} - \mathrm{Min}) + \mathrm{Min} \tag{12}$$

where x represents an element of the data sample features, i.e., the time or the sea/tidal level, and x^* is its normalized value; $x_{\max}$ and $x_{\min}$ are the maximum and minimum values of the corresponding feature among all the data samples used in this study, respectively; Max and Min are the limits of the normalized values, with the values of x^* varying between Min and Max. In this study, $\mathrm{Min} = 0.1$ and $\mathrm{Max} = 1.0$ were set. Notably, all the NaN values in the data sample matrices were set to 0 after the normalization.

IV. Results

A. LSP sea levels

To evaluate the quality of GNSS sea-level estimates derived from the LSP method, we conducted a comparative analysis between the LSP sea-level data and co-located tide-gauge records. Figure 5 displays the time series of those two datasets, superimposed with the astronomical tide. A quantitative summary of the discrepancies between the two datasets is provided in Table 2. We performed the analysis over two distinct periods: (1) the entire 7-day period, and (2) the peak period, defined as the 24-hour interval spanning from 12 hours before to 12 hours after the peak water level. Notably, the period other than the peak period is named hereinafter the normal period. We employed two metrics, i.e., the root-mean-square error (RMSE) and skill score, to assess the performance of the LSP sea levels and our models in subsequent sections. The RMSE is calculated as:

$$\mathrm{RMSE} = \sqrt{\frac{1}{l}\sum_{i=1}^{l}(y_i - y_i')^2} \tag{13}$$

and the skill score is obtained by:

$$\mathrm{Skill} = 1 - \frac{\sum_{i=1}^{l}|y_i - y_i'|^2}{\sum_{i=1}^{l}\left(|y_i - \bar{y}| + |y_i' - \bar{y'}|\right)^2} \tag{14}$$

where y is the real sea level recorded by tide gauge; y' is the sea level obtained from the LSP method or predicted by the SW-LSTM model; l is the number of the predicted data within the considered time span. The RMSE quantifies the average magnitude of the discrepancy between the LSP sea levels and the tide-gauge records, with lower values indicating a better match. The skill score serves as an additional measure of performance, providing a normalized assessment of the model's predictive capability. A skill score value of 1 indicates a prefect prediction.

Overall, the performance of GNSS-IR retrievals using the LSP method was reduced during peak periods, as indicated by generally greater RMSEs and lower skill scores, compared to the entire periods. This reduction is anticipated due to the influence of strong winds during typhoons, which increase sea surface roughness and thus hinder specular reflections. Additionally, heavy rains associated with typhoon events can attenuate the reflected GNSS signals. Consequently, the effectiveness of GNSS-IR is compromised, potentially resulting in an absence of detectable interference patterns in the SNR data and thereby affecting the accuracy of GNSS-IR retrievals. Moreover, the average number of observation points within a given-length window during the peak periods is consistently lower than that during the normal periods (Figure 6).

Moreover, the performance of GNSS-IR retrievals varied across the five typhoon events. The retrieved LSP sea levels in Typhoon Kompasu exhibited the lowest RMSE (14.9 cm) and the highest skill score (97.8%) during the peak period, whereas those in Super Typhoon Mangkhut recorded the highest RMSE (27.3 cm) and the lowest skill score (89.8%). A plausible explanation for this discrepancy is the variation in wind speeds. The maximum wind speed of Super Typhoon Mangkhut reached 171 km/h, significantly exceeding those of the other typhoons [38]. In terms of the results within the entire observation period, the RMSEs for all five events remained below 20 cm, aligning with findings from previous studies conducted at the same site [8], [39], [40]. This consistency underscored the reliability of LSP sea levels in this study.

TABLE II. Performance of GNSS retrievals for sea levels during typhoon Hato, Khanun, Mangkhut, Wipha, and Kompasu.

Typhoon	RMSE (cm)		Skill Score	
	Entire Period	Peak Period	Entire Period	Peak Period
Super Typhoon Hato	18.1	22.9	0.975	0.975
Severe Typhoon Khanun	15.8	16.1	0.963	0.911
Super Typhoon Mangkhut	15.9	27.3	0.972	0.898
Tropical Storm Wipha	18.8	21.7	0.974	0.974
Typhoon Kompasu	15.0	14.9	0.979	0.978

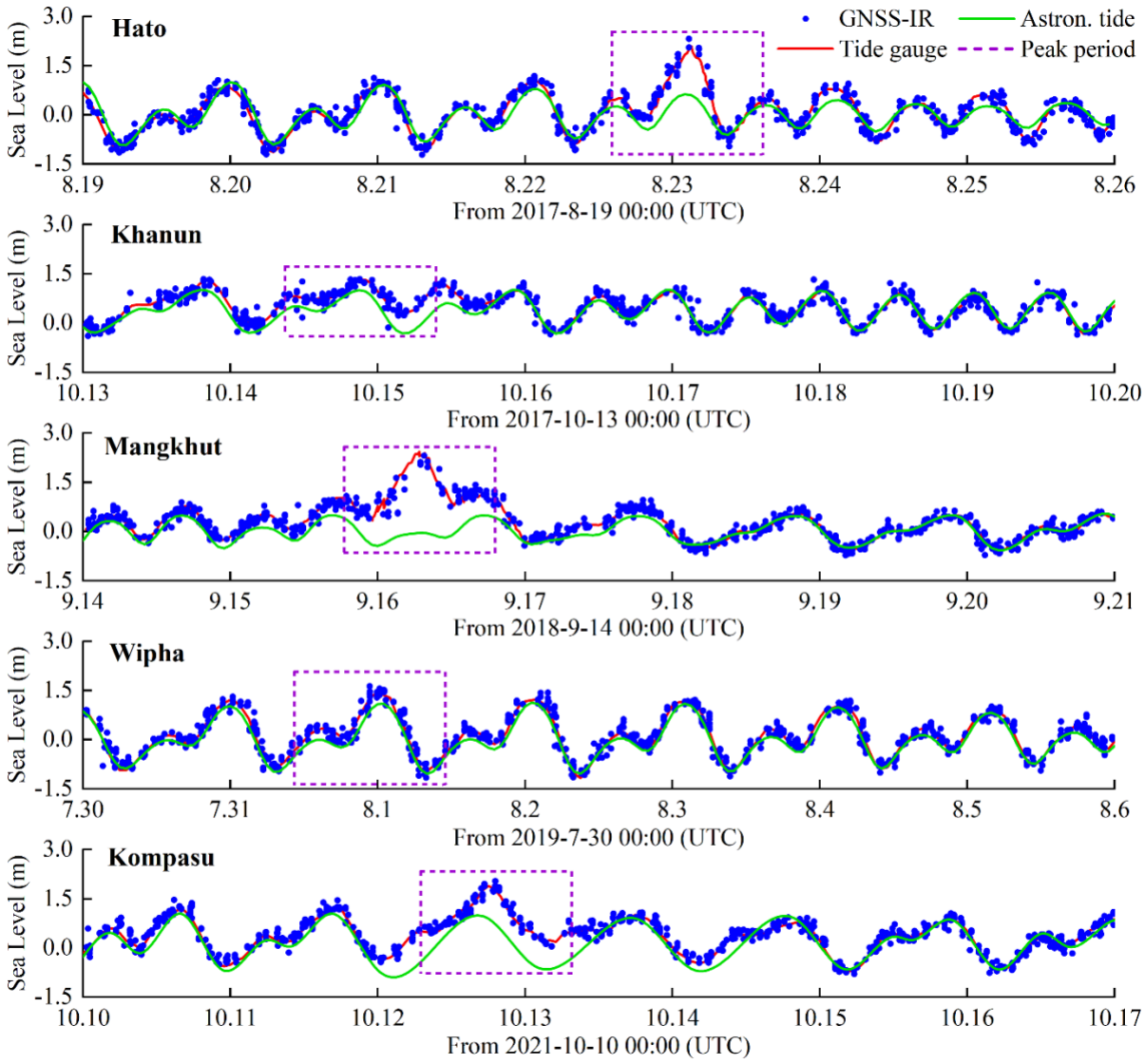

Fig. 5. Comparison between the LSP sea-level measurements (blue dots) and tide-gauge records (red line) at the Quarry Bay station (HKQT) during Hato, Khanun, Mangkhut, Wipha, and Kompasu. The predicted astronomical tide is superimposed (green line). The purple dashes outline the peak periods during each typhoon.

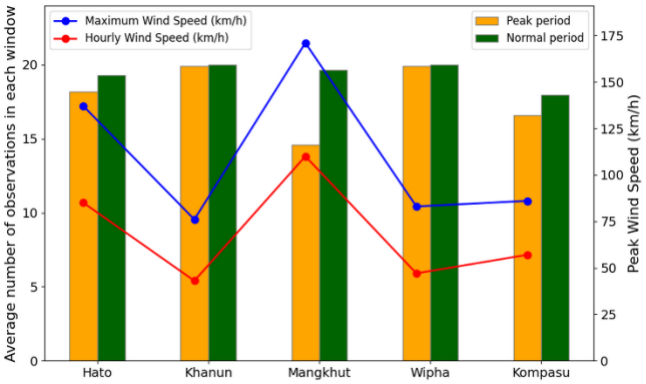

Fig. 6. Comparison of the average numbers of LSP sea level observation points in each sliding window during the peak and normal periods. The maximum gust (blue line) and hourly (red line) wind speeds recorded by the co-located anemometer of the Hong Kong Observatory are superimposed.

B. Enhancing LSP sea levels using SW-LSTM models

We chose the data samples in Mangkhut, Wipha, and Kompasu as the training data of the SW-LSTM network, to establish a mapping function that correlates the LSP sea levels with the real sea level at the target momentum. Subsequently, the model was applied to process the retrieved LSP sea levels to predict a deterministic value of sea level at target moments under typhoons Hato and Khanun. Figures 7 and 8 present the predicted sea-level time series by the three scenarios of the SW-LSTM model in Hato and Khanun, respectively. In the figures, the LSP sea levels, the tide-gauge records, and the astronomical tide are superimposed.

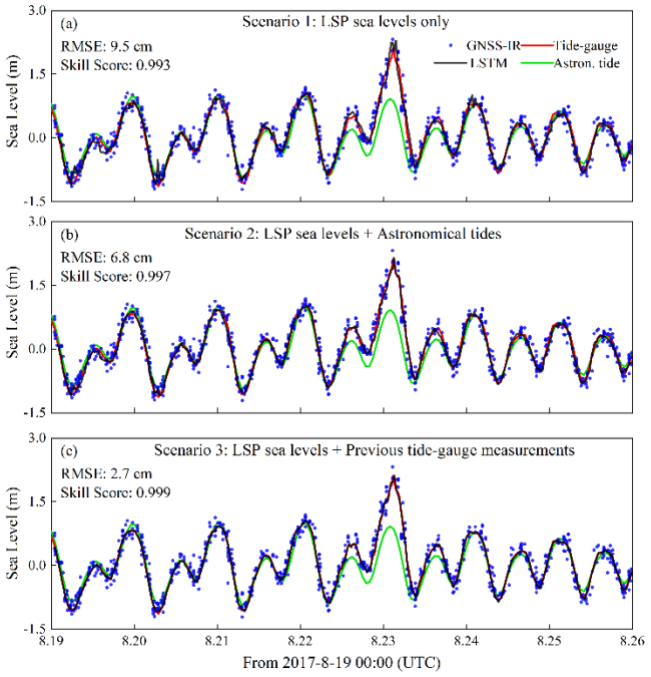

Fig. 7. The predicted sea levels during Hato by the three scenarios of the SW-LSTM model. The values of RMSE and skill score in the predicted results during the entire concerned period, relative to the real sea levels recorded by the tide gauge (red curves), are included. The retrieved LSP sea levels (blue dots) and the astronomical tide (green curves) are superimposed.

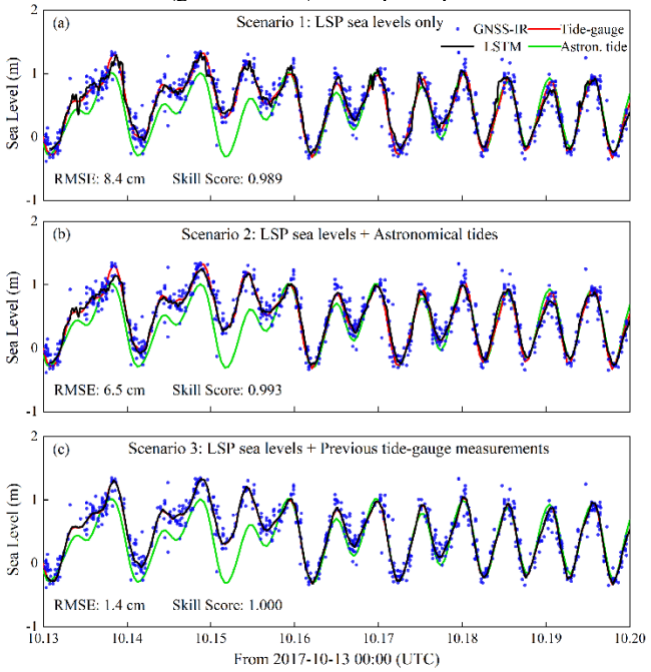

Fig. 8. The predicted sea levels during Khanun by the three scenarios of the SW-LSTM model. The values of RMSE and skill score in the predicted results during the entire concerned period, relative to the real sea levels recorded by the tide gauge (red curves), are included. The retrieved LSP sea levels (blue dots) and the astronomical tide (green curves) are superimposed.

Compared to the LSP sea levels, the sea levels predicted using the SW-LSTM models show signifciantly better agreement with the co-located tide-gauge records during both the peak and normal periods. Over the entire 7-day periods, the RMSE decreased from 18.1 cm in the LSP retrieval data to 9.5 cm in the results of the first SW-LSTM scenario for Hato and from 15.8 cm to 8.4 cm for Khanun. Upon incorporating the astronomical tide (Scenario 2), the RMSE further decreased to 6.8 cm in the results of the second SW-LSTM scenario for Hato and 6.5 cm for Khanun. When using the previous tide-gauge records as the prior information (Scenario 3), the RMSE was reduced to 2.7 cm in the results of the third SW-LSTM scenario for Hato and 1.4 cm for Khanun. The skill scores in the results of the entire period were also improved, approaching 1.000.

For the sea level observation during the peak periods, the improvement over the original LSP sea levels achieved by post-processing with the SW-LSTM models is significant, even though less satisfactory compared to that for the normal periods. For Super Typhoon Hato, the RMSE improved from 22.9 cm in the originally retrieved LSP sea levels to 14.4 cm in the predictions of Scenario 1, to 8.6 cm in those of Scenario 2, and to 4.6 cm in those of Scenario 3. For Severe Typhoon Khanun, the RMSE improved from 16.1 cm to 7.5 cm in the predictions of Scenario 1, to 5.1 cm of Scenario 2, and to 1.3 cm of Scenario 3. The corresponding skill scores also improved. Additionally, the SW-LSTM models performed better for Khanun across both the enrire and peak periods. The most likely reason for this is the higher quality of the input originally retrieved LSP sea levels in the case of Khanun, suggesting that the SW-LSTM models rely heavily on the quality of the input data.

C. Sensitivities to the window length of SW-LSTM models

The length of the sliding window is a crucial parameter influencing the accuracy of the SW-LSTM models. Figure 9 shows the results of the sensitivity study on the sliding window length. The values of the RMSE in the predictions of the first SW-LSTM scenario for sea levels in the entire period during Khanun varied non-monotonically. Specifically, the RMSE decreased as the window length increased from 2 hours to 4 hours and then increased when extending the window length beyond 4 hours. A 4-hour window length optimizes the performance of SW-LSTM models. Therefore, in this study, we used a length of 4 hours for the sliding windows.

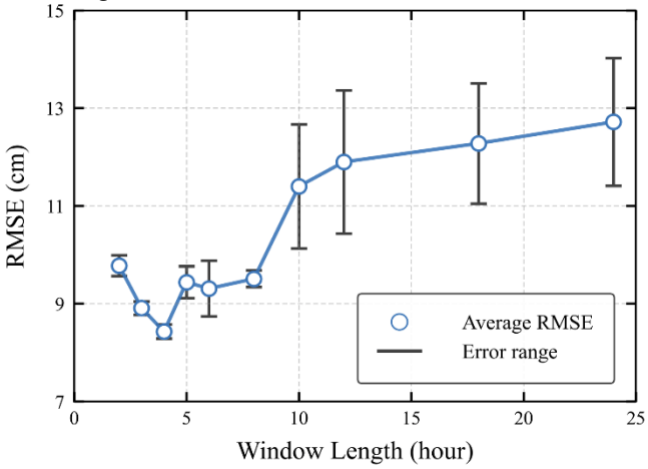

Fig. 9. The variation of the RMSE in the predictions of the first SW-LSTM scenario for sea levels in the entire period during Khanun with the window length.

V. Discussion

The LSP sea levels obtained using GNSS-IR have been widely applied to sea-level related investigations, including studies on tides [41]-[43], storm surges [8], [44], tsunamis [45], [46] and seasonal sea-level cycles [47], [48]. Despite their widespread applications, the temporal resolution and accuracy of these measurements are inherently constrained by factors such as the frequency of satellite overflights, the precision of the SNR data, and the geometric characteristics of the specific site [49]. To enhance the temporal resolution and accuracy, [50] introduced an inverse modeling technique, which represented sea surface heights as a continuous function using B-splines. That method yielded more accurate and continuous sea-level time series, but it suffered from a low computational efficiency. To overcome this limitation, reference [51] proposed a technique that fitted the LSP sea levels with a cubic spline in sliding windows. Similar methods, including other inverse techniques based on least squares, have also been developed [27], [39], [52], [53]. Compared to previous inverse methods, both the post-processing spline method and least squares inverse methods rely on spectral techniques, such as LSP or wavelet analysis [54], which retain high accuracy while significantly improving computational efficiency.

This study specifically examines storm surge periods, during which the LSP sea levels exhibit more outliers and larger deviations compared with normal conditions. These anomalies present a significant challenge for traditional post-processing techniques. However, the SW-LSTM post-processing approach provides an open framework that effectively handles outliers and integrates multiple influencing factors. This method avoids the need for complex and time-consuming physical calculations, offering a more efficient and robust solution for analyzing sea level data during storm surges and achieving higher accuracy compared to others.

A. Comparison between SW-LSTM, Least-Square Method, and Cubic Spline Method

Least square method (LSM) is a standard approach in regression analysis to approximate the solutions for overdetermined systems. It achieves the optimization by minimizing the sum of the squares of residuals, which are the differences between observed and calculated values. Because of its simplicity and ease of interpretation, the LSM has been adopted in post processing LSP sea levels [27], [52]. However, LSM assumes a linear relationship between variables, which may not be accurate in complex scenarios. Additionally, it is sensitive to outliers, which can significantly skew results. It may also overfit the data if the model becomes too complex.

We employed the LSM optimization method proposed by [27], which additionally considers tropospheric delay following [52]. In the method, the variation rate of sea level, quantified by $\dot{h} = dh/dt$, is considered in the inversion of reflector height. Firstly, the sliding windows are also adopted and the LSM method aims to yield the reflector height h and its variation rate $\dot{h}$ at the central moment of each window. According to the reflector height retrieval theory, there is a relationship between the LSP result and a linear combination of h and $\dot{h}$, expressed as

$$\bar{h} = \frac{\tan(\varepsilon)}{\dot{\varepsilon}}\dot{h} + h \tag{15}$$

where $\bar{h}$ is the result of the reflector height obtained from the LSP method using the gnssrefl software package of [31], which has included the tropospheric height correction; $\dot{\varepsilon}$ is the variation rate of the satellite elevation angle ε. Considering the *i*-th sliding window, if there are n data points retrieved from the LSP method, the above relationship is further written as

$$\bar{h}_i = U_i \dot{h}_i + h_i \tag{16}$$

where

$$\bar{h}_i = \begin{bmatrix} \bar{h}_{i,1} \\ \vdots \\ \bar{h}_{i,j} \\ \vdots \\ \bar{h}_{i,n} \end{bmatrix} \tag{17}$$

$$U_i = \begin{bmatrix} \dfrac{\tan(\varepsilon_{i,1})}{\dot{\varepsilon}_{i,1}} + T_{i,1} - T_i \\ \vdots \\ \dfrac{\tan(\varepsilon_{i,j})}{\dot{\varepsilon}_{i,j}} + T_{i,j} - T_i \\ \vdots \\ \dfrac{\tan(\varepsilon_{i,n})}{\dot{\varepsilon}_{i,n}} + T_{i,n} - T_i \end{bmatrix} \tag{18}$$

in which $\bar{h}_{i,j}$ ($j = 1, \ldots, n$) is the result of the *j*-th LSP-derived data point in the *i*-th window and $T_{i,j}$ is its corresponding moment; T_i is the central moment of the *i*-th window. Further, Eq. (16) is rewritten into

$$\bar{h}_i = V_i Z_i \tag{19}$$

where the matrix $V_i = [U_i, \mathbf{1}_{n\times 1}]$ and $Z_i = [\dot{h}_i, h_i]^{\mathrm{T}}$; $\mathbf{1}_{n\times 1}$ is a ones vector with a dimension of $n\times 1$. Using the least squares method, the real reflector height h_i and its variation rate $\dot{h}_i$ at the central moment of the *i*-th sliding window are calculated as

$$[\dot{h}_i, h_i]^{\mathrm{T}} = Z_i = \left(V_i^{\mathrm{T}} V_i\right)^{-1} V_i^{\mathrm{T}} \bar{h}_i . \tag{20}$$

Accordingly, once the reflector height is obtained, the sea level at the window central moment is acquired by subtracting h_i from the GNSS antenna height.

For comparison with the results from our SW-LSTM model, in the LSM optimization, we also utilized a window length of 4 hours and a sliding interval of 15 minutes. Based on the LSP retrieved results, the LSM method was utilized to obtain new time series of sea levels during the entire period of Hato and Khanun, as shown in Figure 10. Firstly, we validated the implementation of the LSM method in terms of the results during Hato. Reference [39] adopted the LSM method to retrieve sea level at HKQT station during Hato, achieving a

RMSE ranging from 7.6 cm to 21.53 cm for different frequencies of quad-constellations. Our LSM results yield an RMSE of 10.7 cm and aligns with the level of accuracy, thereby demonstrating the effectiveness of the LSM implementation in this study.

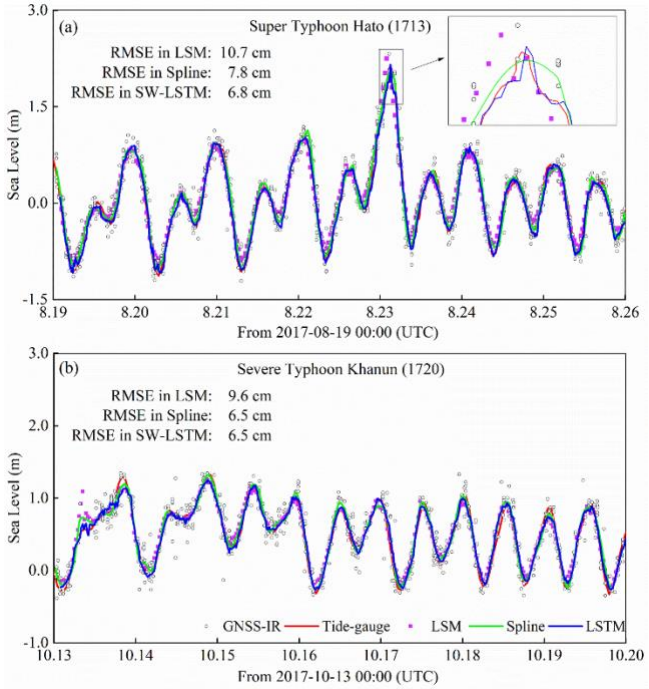

Fig. 10. Comparison between the time series of sea levels during (a) Hato and (b) Khanun obtained using the LSM method, the Spline interpolation, and the second scenario of SW-LSTM model.

Additionally, we employed the cubic spline interpolation approach, utilizing the open-source code provided in [51], to fit the LSP retrieved data and obtained new time series of sea levels. These results are compared with those obtained from the second scenario of our SW-LSTM model in Figure 10. Overall, in this study, the three methods all demonstrate high accuracy for storm surge inversion at the HKQT station, achieving results that are comparable to or exceed the accuracy levels reported in previous studies [25], [53]. Comparatively, the LSM method performs worst among the three approaches in both typhoons while our SW-LSTM model performed best. The performance of the cubic spline interpolation is comparable to the SW-LSTM model in the Severe Typhoon Khanun but the RMSE in its results in Super Typhoon Hato is larger than that of our SW-LSTM model. The spline interpolation tends to smooth water levels, which results in the loss of detail, particularly at the peaks of sea levels. As shown in the inset of Figure 10(a), the large rising gradient of sea level cannot be reproduced by the spline interpolation. In comparison, our SW-LSTM model is more effective in capturing these rapid variations. In the inset, the sensitivity of the LSM method to outliers is also shown, which results in the overestimation of the peak sea level.

B. Temporal resolution and duplicate values

The number of retrieved LSP sea levels in each sliding window is not constant, as shown in Figure 11. Within a 4-hour window, the number of LSP data points generally fluctuates between 10 and 40. Additionally, multi-frequency signals can introduce multiple LSPs simultaneously, making it challenging to accurately determine the true water level. Previous studies, such as [55], [56] proposed two filtering approaches to enhance the retrieval accuracy: using a reliable signal and averaging the retrieval results from different frequencies. However, both filtering approaches have inherent limitations. The optimal signal is not consistently fixed, and the mean fusion only provides an average value. If multiple points are biased to one side, this method can exacerbate errors. Moreover, the temporal resolution after filtering the duplicate points, as indicated by the black lines in Figure 11, is low and insufficient for storm surge monitoring. Our SW-LSTM model circumvents the issue of separating duplicate points by integrating all nearby LSP values in the model training.

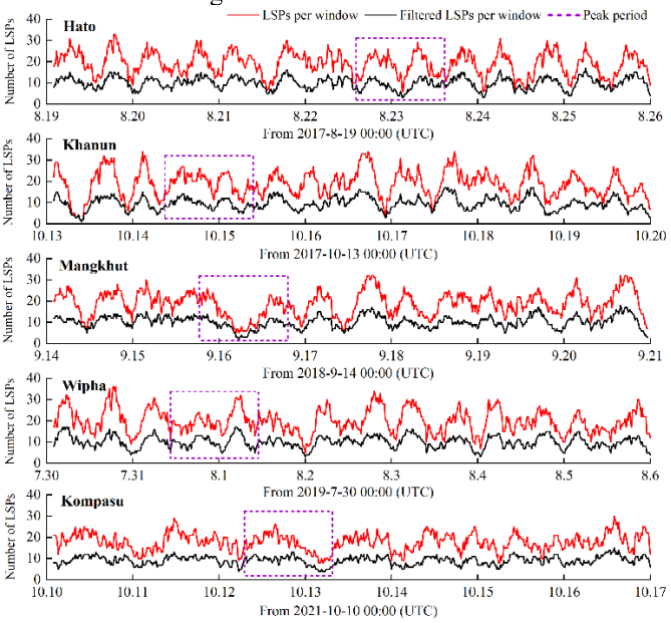

Fig. 11. The variation of the temporal resolution of retrieved LSP sea levels, quantified by the number of LSP data points in each 4-hour sliding window, in the five typhoon cases. The red lines refer to the number of original retrieved LSP sea levels per window, and the black lines show the number of LSP sea levels after filtering duplicate retrieval results.

C. Limitation and future direction

Our study has several limitations. Even though we have achieved high accuracy in the time series of sea level during Hato and Khanun, the number of the training dataset is limited. Typically, a rate between the training and test data is greater than 8:2, whereas our study employed a ratio of 3:2 primarily due to the limited available dataset. More data samples under normal conditions and different categories of typhoons may help to fully train the model, capture the properties among the data, and further increase the measurement accuracy. Another limitation is the inherent variability of machine learning models, that is, the output of each model training varies slightly and the final yielded result of a specific sea level fluctuates with a range of about ± 1.5 cm.

Our SW-LSTM models provide an open framework for the GNSS-IR field. First, it can be used for real-time water level

monitoring and synchronous prediction (Figure 12). The target output of the SW-LSTM model can be the sea level at the current time for real-time monitoring or at a future moment for prediction. Second, there may be improvements of the current model structure for more complex applications, such as increasing convolutional neural network (CNN) layers to extract spatial relationships between data obtained from several neighboring GNSS-IR retrievals. Third, incorporating additional factors such as wind and air pressure may improve the results, especially during storm surges, as water levels are highly influenced by wind and air pressure in coastal areas. The SW-LSTM framework allows us to bypass some physical derivations and integrate these factors effectively.

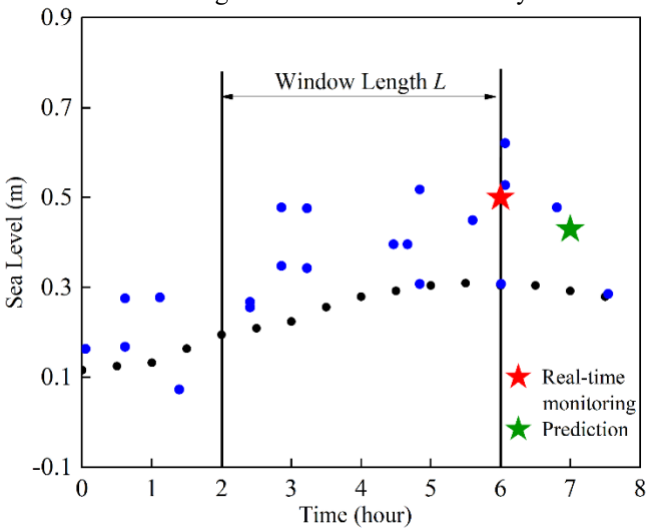

Fig. 12. Sketch of the outputs of SW-LSTM model for real-time monitoring and prediction. If the target output of the SW-LSTM model is the sea level at the end of the window (the red star), the model can be applied to real-time sea level monitoring; if the target output is the sea level at a future moment (the green star), the model can be applied to prediction of future sea level.

VI. Conclusion

Storm surge observation requires high temporal resolution and accuracy. We aim to achieve both by using an SW-LSTM machine learning model to post-process GNSS-IR retrieved sea levels. The multi-satellites and multi-frequencies technique was adopted to enhance the retrieved results using the LSP algorithm. The 7-day time series of sea levels at the HKQT station in the Quarry Bay of Hong Kong during five typhoons were obtained from the LSP analysis on GNSS SNR data. The RMSEs in the obtained sea levels varied between 15.0 cm and 18.8 cm during the 7-day periods while increased up to 27.3 cm during the peak period under the Super Typhoon Mangkhut.

An SW-LSTM model was developed to post-process the LSP sea levels, which is composed of a multi-layer LSTM neural network and a data-combination component using the sliding window. The target output of the LSTM neural network is the sea level at the central moment of a sliding window and its input features are all the retrieved LSP sea levels as well as some prior information within the corresponding window. In terms of the adopted prior information, three scenarios of the SW-LSTM model were defined. In SW-LSTM Scenario 1, no prior information is involved; In SW-LSTM Scenario 2, the predicted local astronomical tide is adopted as the prior information; In SW-LSTM Scenario 3, the neighboring tide-gauge measurements of sea levels before the window central moment are utilized as the prior information. The data samples in typhoons Mangkhut, Wipha, and Kompasu were employed for model training and the time series of sea levels in Hato and Khanun were applied to examine the model performance. The RMSE in the retrieved LSP sea levels during the peak period in the Super Typhoon Hato was 22.9 cm, while the values of RMSE in the post-processed sea level time series by the SW-LSTM Scenarios 1, 2, and 3 were 14.4 cm, 8.6 cm, and 4.6 cm, respectively. Similarly, the RMSE in the retrieved LSP sea levels during the peak period in the Severe Typhoon Khanun was significantly reduced from 16.1 cm to 7.5 cm in the results of Scenario 1, 5.1 cm of Scenario 2, and 1.3 cm of Scenario 3.

Moreover, we compared the performance of the SW-LSTM model with those of another two methods that are currently popular for improving the GNSS-IR retrieval accuracy, i.e., the least squares method (LSM) and the cubic spline interpolation. The results illustrate that the SW-LSTM model achieves the highest accuracy and provides the best fit for abrupt changes during storm surge peaks. It effectively captures the detailed process of abnormal water level increases, close to the real tide gauge records.

Acknowledgment

The authors appreciate the GNSS data provided by Geodetic Survey Section Survey and Mapping Office, Lands Department at https://www.geodetic.gov.hk/tc/rinex/downv.aspx.

References

[1] H. M. Fritz et al., "Hurricane Katrina storm surge distribution and field observations on the Mississippi Barrier Islands. Estuarine," *ESTUAR COAST SHELF S.,* vol. 74, no. 1-2, pp. 12-20, May. 2007, doi: 10.1016/j.ecss.2007.03.015.

[2] J. L. A. Soria et al., "Repeat storm surge disasters of Typhoon Haiyan and its 1897 predecessor in the Philippines," *Bull. Am. Meteorol. Soc.,* vol. 97, no. 1, pp. 31-48, Jan. 2016, doi: 10.1175/BAMS-D-14-00245.1.

[3] R. Nakamura, T. Shibayama, M. Esteban, and T. Iwamoto, "Future typhoon and storm surges under different global warming scenarios: case study of typhoon Haiyan (2013)," *Nat. Hazards,* vol. 82, pp.1645-1681, Feb. 2016, doi: 10.1007/s11069-016-2259-3.

[4] S. Rahmstorf, "Rising hazard of storm-surge flooding," *Proc. Natl. Acad. Sci.,* vol. 114. no. 45, pp. 11806-11808, Oct. 2017, doi: 10.1073/pnas.1715895114.

[5] W. Matthäus, "On the History of Recording Tide Gauges," *Proc. R. Soc. Edinb. Biol.,* vol. 73, pp. 26-34, 1972, doi: 10.1017/S0080455X00002083.

[6] P. L. Woodworth, J. M. Vassie, R. Spencer, and D. E. Smith, "Precise datum control for pressure tide gauges," *Mar. Geodesy,* vol. 19, no. 1, pp. 1-20, Jul. 1996, doi: 10.1080/01490419609388068.

[7] R. M. Heitsenrether, W. M. Hensley, and J. D. Boon, "Results from NOAA's test and evaluation of microwave radar water level sensors and plans for a transition to operational applications," in *OCEANS'11 MTS/IEEE KONA,* Waikoloa, HI, USA, 2011, pp. 1-10, doi: 10.23919/OCEANS.2011.6107140.

[8] D. Peng, E. M. Hill, L. Li, A. D. Switzer, and K. M. Larson, "Application of GNSS interferometric reflectometry for detecting storm surges," *GPS Solutions*, vol. 23, pp. 1-11, 2019, doi: 10.1007/s11069-016-2259-3.

[9] L. Li *et al.,* "Field survey of Typhoon Hato (2017) and a comparison with storm surge modeling in Macau," *Nat. Hazards Earth Syst. Sci.,* vol. 18, no. 12, pp. 3167-3178, Nov. 2018, doi: 10.5194/nhess-18-3167-2018.

[10]J. Yang *et al.,* "A comparative study of Typhoon Hato (2017) and Typhoon Mangkhut (2018) - Their impacts on coastal inundation in Macau," *J. GEOPHYS RES-OCEANS,* vol. 124, no. 12, pp. 9590-9619, Dec. 2019, doi: 10.1029/2019JC015249.

[11]K. M. Larson, R. D. Ray, F. G. Nievinski, and J. T. Freymueller, "The accidental tide gauge: a GPS reflection case study from Kachemak Bay, Alaska," *IEEE Geosci. Remote Sens. Lett.,* vol. 10, no. 5, pp. 1200-1204, Feb. 2013, doi: 10.1109/LGRS.2012.2236075.

[12]K. M. Larson, J. S. Löfgren, and R. Haas, "Coastal sea level measurements using a single geodetic GPS receiver," *Adv. Space Res.,* vol. 51, no. 8, pp. 1301-1310, Apr. 2013, doi: 10.1016/j.asr.2012.04.017.

[13]C. Roesler, and K. M. Larson, "Software tools for GNSS interferometric reflectometry (GNSS-IR)," *GPS Solutions*, vol. 22, no. 3, Jun. 2018, Art. no. 80, doi: 10.1007/s10291-018-0744-8.

[14]K. Srisutha, and J. Park, "GNSS Interferometric Reflectometry as an Operational Framework for Real-Time Tide Estimation," *J. SURV ENG-ASCE*, vol. 151, no. 2, Mar. 2025, Art. no. 04025004, doi: 10.1061/JSUED2.SUENG-1545.

[15]A. Santamaría-Gómez, C. Watson, M. Gravelle, M. King, and G. Wöppelmann, "Levelling co-located GNSS and tide gauge stations using GNSS reflectometry," *J. Geodesy,* vol. 89, no. 3, pp. 241-258, Dec. 2014, doi: 10.1007/s00190-014-0784-y.

[16]D. Peng, L. Feng, K. M. Larson, and E. M. Hill, "Measuring coastal absolute sea-level changes using GNSS interferometric reflectometry," *Remote Sens.,* vol. 13, no. 21, Sep. 2021, Art. no. 4319, doi: 10.3390/rs13214319.

[17]S. Hochreiter, and J. Schmidhuber, "Long short-term memory," *Neural Comput.*, vol. 9, no. 8, pp. 1735-1780, Nov. 1997, doi: 10.1162/neco.1997.9.8.1735.

[18]A. Ghosh, S. Bose, G. Maji, N. Debnath, and S. Sen, "Stock price prediction using LSTM on Indian share market," In *Proceedings of 32nd international conference*, vol. 63, pp. 101-110, 2019, doi: 10.29007/qgcz.

[19]S., Liu, G. Liao, and Y. Ding, "Stock transaction prediction modeling and analysis based on LSTM," in *2018 13th IEEE Conference on Industrial Electronics and Applications (ICIEA)*, Wuhan, China, pp. 2787-2790. Jun. 2018, doi: 10.1109/ICIEA.2018.8398183.

[20]I. M. Baytas, C. Xiao, X. Zhang, F. Wang, A. K. Jain, and J. Zhou, "Patient subtyping via time-aware LSTM networks," in *Proceedings of the 23rd ACM SIGKDD international conference on knowledge discovery and data mining*, pp. 65-74, Aug. 2017, doi: 10.1145/3097983.3097997.

[21]G. Nearing *et al.,* "Global prediction of extreme floods in ungauged watersheds," *Nature*, vol. 627, pp. 559–563, Mar. 2024, doi: 10.1038/s41586-024-07145-1.

[22]X. Liu *et al.,* "FA-RDN: A hybrid neural network on GNSS-R sea surface wind speed retrieval," *Remote Sens.,* vol. 13, no. 23, Nov. 2021, Art. no. 4820, doi: 10.3390/rs13234820.

[23]N. Limsupavanich, B. Guo, and X. Fu, "Improvement of coastal sea-level altimetry derived from GNSS SNR measurements using the SNR forward network and T-LSTM anomaly detection," *IEEE Trans. Geosci. Remote Sens.,* vol, 60, pp. 1-13, Jun. 2022, doi: 10.1109/TGRS.2022.3186239.

[24]S. Gholamrezaee, M. Bagherbandi, K. Parvazi, and S. Farzaneh, "A study on the quality of GNSS signals for extracting the sea level height and tidal frequencies utilizing the GNSS-IR approach," *GPS Solutions*, vol. 27, no. 2, Feb. 2023, Art. no. 72, doi: 10.1007/s10291-023-01416-6.

[25]R. Li, Y. Wen, X. Wang, and H. Xu, "Multi-GNSS combination multipath reflectometry based on IVMD method for sea level retrieval," *Remote Sens.,* vol. 15, no. 7, Mar. 2023, Art. no. 1733, doi: 10.3390/rs15071733.

[26]D. Peng, Y. N. Lin, J. C. Lee, H. H. Su, and E. M. Hill, "Multi-constellation GNSS interferometric reflectometry for tidal analysis: mitigations for K1 and K2 biases due to GPS geometrical errors," *J. Geodesy,* vol. 98, no. 1, Jan. 2024, Art. no. 5, doi: 10.1007/s00190-023-01812-3.

[27]X. Wang, X. He, and Q. Zhang, "Evaluation and combination of quad-constellation multi-GNSS multipath reflectometry applied to sea level retrieval," *Remote Sens. Environ.,* vol. 231, Jun. 2019, Art. no. 111229, doi: 10.1016/j.rse.2019.111229.

[28]X. Yuan, Y. Hu, W. Liu and J. Wickert, "GNSS-IR Snow Depth Retrieval Based on the PSO-NFP Method With Multi-GNSS Constellations," *IEEE Trans. Geosci. Remote Sens.*, vol. 62, pp. 1-10, Nov. 2024, Art. no. 5802810, doi: 10.1109/TGRS.2024.3492495.

[29]H. Chai, and K. Chen, "Facilitated interferometric reflectometry evaluation and its application in monitoring three typhoon storm surges in Hong Kong with multi-GNSS constellation," *GPS Solutions*, vol. 28, no. 3, Apr. 2024, Art. no. 99, doi: 10.1007/s10291-024-01642-6.

[30]R. E. Phelts, and D. M. Akos, "Range biases on modernized GNSS codes," in *Proceedings of the European Navigation Conference GNSS/TimeNav,* 2007.

[31]K. M. Larson, "Gnssrefl: an open source software package in python for GNSS interferometric reflectometry applications." *GPS Solutions*, vol. 28 no. 4, Jul. 2024, Art. No. 165, doi: 10.1007/s10291-024-01694-8.

[32]T. Nikolaidou, M. C. Santos, S. D. P. Williams, and F. Geremia-Nievinski, "Raytracing atmospheric delays in ground-based GNSS reflectometry," *J. Geodesy,* vol. 94, no. 8, Jul. 2020, Art. no. 68, doi: 10.1007/s00190-020-01390-8.

[33]A. Santamaría-Gómez, and C. Watson, "Remote leveling of tide gauges using GNSS reflectometry: case study at Spring Bay, Australia," *GPS Solutions*, vol. 21, pp. 451-459, Apr. 2016, doi: 10.1007/s10291-016-0537-x.

[34]S. D. P. Williams, and F. G. Nievinski, "Tropospheric delays in ground-based GNSS multipath reflectometry — Experimental evidence from coastal sites," *J. GEOPHYS RES-SOL EA,* vol. 122, no. 3, pp. 2310-2327, Mar. 2017, doi: 10.1002/2016JB013612.

[35]G. G. Bennett, "The calculation of astronomical refraction in marine navigation," *J. Navig.,* vol. 35, no. 2, pp. 255-259. 1982, doi: 10.1017/S0373463300022037.

[36]J. Böhm, G. Möller, M. Schindelegger, G. Pain, and R. Weber, "Development of an improved empirical model for slant delays in the troposphere (GPT2w)," *GPS Solutions*, vol. 19, pp. 433-441, Aug. 2014, doi: 10.1007/s10291-014-0403-7.

[37]P. Feng, R. Haas and G. Elgered, "A Novel Tropospheric Error Formula for Ground-Based GNSS Interferometric Reflectometry," *IEEE Trans. Geosci. Remote Sens.,* vol. 61, pp. 1-18, 2023, Art no. 5802918, doi: 10.1109/TGRS.2023.3332422.

[38]X. Wang, Y. Nan, M. Song and X. He, "Incoherent GNSS-IR Model and Its Application in Wind Speed Retrieval," *IEEE Trans. Geosci. Remote Sens.,* vol. 62, pp. 1-8, 2024, Art no. 5803208, doi: 10.1109/TGRS.2024.3505604.

[39]X. Wang, Z. Niu, S. Chen, and X. He, "A correction method of height variation error based on one SNR arc applied in GNSS–IR sea-level retrieval," *Remote Sens.,* vol. 14, no. 1, Dec. 2021, Art. no. 11, doi: 10.3390/rs14010011.

[40]N. Wang *et al.,* "Sea-level monitoring and ocean tide analysis based on multipath reflectometry using received strength indicator data from multi-GNSS signals," *IEEE Trans. Geosci. Remote Sens.,* vol. 60, pp. 1-13, Nov. 2022, doi: 10.1109/TGRS.2022.3219074.

[41]S. Gholamrezaee, M. Bagherbandi, K. Parvazi, and S. Farzaneh, "A study on the quality of GNSS signals for extracting the sea level height and tidal frequencies utilizing the GNSS-IR approach," *GPS Solutions*, vol. 27, Feb. 2023, Art. no. 72, doi: 10.1007/s10291-023-01416-6.

[42]M. Rajabi *et al.,* "Tidal harmonics retrieval using GNSS-R dual-frequency complex observations," *J. Geodesy,* vol. 97, no. 10, Oct. 2023, Art. no. 94, doi: 10.1007/s00190-023-01782-6.

[43]I. Sepúlveda, B. Cao, J. S. Haase, and M. J. Murphy Jr, "Optimizing Simultaneous Water Level and Wave Measurements From Multi-GNSS Interferometric Reflectometry Over 1 Year at an Exposed Coastal Site," *Earth and Space Science,* vol. 10, no. 6, Jun. 2023, Art. no. e2022EA002767, doi: 10.1029/2022EA002767.

[44]F. A. Oreiro, and M. M. E. Fiore, "Water level measurement with a low-cost smartphone using GNSS-IR: an over 2-year study case in Buenos Aires, Argentina," *GPS Solutions*, vol. 28, no. 4, Jul. 2024, Art. no. 163, doi: 10.1007/s10291-024-01710-x.

[45]K. M. Larson *et al.,* "Dynamic sea level variation from GNSS: 2020 Shumagin earthquake tsunami resonance and Hurricane Laura," *Geophys. Res. Lett.,* vol. 48, no. 4, Dec. 2020, Art. no. e2020GL091378, doi: 10.1029/2020GL091378.

[46]L. Li *et al.*, "Island-based GNSS-IR network for tsunami detecting and warning," *COAST ENG*, vol. 190, Jun. 2024, Art. no. 104501, doi: 10.1016/j.coastaleng.2024.104501.

[47]K. Ansari, "Review on role of multi-constellation global navigation satellite system-reflectometry (GNSS-R) for real-time sea-level measurements," in *Mukherjee, S. (eds) Structural Geology and Tectonics Field Guidebook, Springer Geology,* Cham, Springer, 2023, vol. 2, pp. 333-358.

[48]D. Peng *et al.,* "Tidal asymmetry and transition in the Singapore Strait revealed by GNSS interferometric reflectometry," *Geosci. Lett.,* vol. 10, no. 1, Aug. 2023, Art. no. 39, doi: 10.1186/s40562-023-00294-7.

[49]K. M. Larson, R. D. Ray, and S. D. Williams, "A 10-year comparison of water levels measured with a geodetic GPS receiver versus a conventional tide gauge," *J. Atmos. Oceanic Technol.,* vol. 34, no. 2, pp. 295-307, Feb. 2017, doi: 10.1175/JTECH-D-16-0101.1.
[50]J. Strandberg, T. Hobiger, and R. Haas, "Improving GNSS-R sea level determination through inverse modeling of SNR data," *Radio Sci.,* vol. 51, no. 8, pp. 1286-1296, Aug. 2016, doi: 10.1002/2016RS006057.
[51]D. Purnell, N. Gomez, W. Minarik, and G. Langston, "Real-time water levels using GNSS-IR: A potential tool for flood monitoring," *Geophys. Res. Lett.,* vol. 51, no. 5, Feb. 2024, Art. no. e2023GL105039, doi: 10.1029/2023GL105039.
[52]N. Roussel *et al.,* "Sea level monitoring and sea state estimate using a single geodetic receiver," *Remote Sens. Environ.,* vol. 171, pp. 261-277. Nov. 2015, doi: 10.1016/j.rse.2015.10.011.
[53]J. Hou, N. Wang, K. He, F. Gao, and S. Wang, "Comparative analysis of GNSS-IR sea-level retrieval methods," *Meas. Sci. Technol.,* vol. 35, no. 5, Feb. 2024, Art. no. 055116, doi: 10.1088/1361-6501/ad2967.
[54]F. Gao, H. Hu, L. Liu, G. Wang, and H. Sun, "Utilizing Normal Time-Frequency Transform-Assisted GNSS-R to Retrieve Sea Surface Height," *IEEE Trans. Geosci. Remote Sens.*, vol. 62, pp. 1-14, Aug. 2024, doi: 10.1109/TGRS.2024.3445461.
[55]J. Tu *et al.,* "GNSS-IR snow depth retrieval from multi-GNSS and multi-frequency data," *Remote Sens.,* vol. 13, no. 21, Oct. 2021, Art. no. 4311, doi: 10.3390/rs13214311.
[56]N. Wang *et al*., "Soil Moisture Estimation Based on GNSS-R Using L5 Signals From a Quasi-Zenith Satellite System," *IEEE Geosci. Remote Sens. Lett.,* vol. 19, pp. 1-5, May. 2022, Art. no. 2505005, doi: 10.1109/LGRS.2022.3176463.

Kailun Hu received the B.Sc. degree in Water Resources and Hydropower Engineering from Hebei University of Engineering, Handan, China and the M.S. degree in hydraulics and environmental engineering from University of Macau, Macao, China. He is currently pursuing the Ph.D. degree with the GNSS applications in state key laboratory for internet of things for smart city, University of Macau, Macao, China, focusing his research in sea level estimation based on global navigation satellite system interferometric reflectometry (GNSS-IR) and coastal disasters.

Dongju Peng received the B.Sc. degree in geodesy and geomatics from the Wuhan University, Wuhan, China, and the Ph.D. degree in astrometry and celestial mechanics from the University of Chinese Academy of Sciences, Beijing, China. She is a Research Assistant Professor with the Department of Department of Land Surveying and Geo-Informatics, The Hong Kong Polytechnic University, Hong Kong, China. She is a geodesist. Her research interests include primarily the detection and attribution of regional sea-level changes, study coastal sea-level rise in and around Southeast Asia and the associated impacts of climate change, natural hazards, and human interventions.

Linlin Li received the B.Sc. degree in Hydraulic Engineering: Department of Environment and Water Conservancy Engineering, Zhengzhou University, China, and the Ph.D. degree in Hydraulic Engineering: Department of Hydraulic Engineering, Tsinghua University, Beijing, China.
Shi is a Professor with the Department of Earth Sciences and Engineering, Sun Yat-Sen University, Zhuhai, China. Her research interests include quantitative analysis of key factors affecting the tsunamigenic potential of submarine earthquakes and application of the GNSS-IR technology in monitoring extreme sea level changes.

Huabin Shi received the B.Sc. degree and Ph.D. degree in Hydraulic Engineering, Tsinghua University, Beijing, China.
He is an Assistant Professor with State Key Laboratory of Internet of Things for Smart City and Department of Ocean Science and Technology, University of Macau, Macao, China. His research interests include coastal hydrodynamic hazards, focusing on storm surge and tsunami, sediment dynamics and granular flows in natural phenomena and hazards.